## **ENGINEERING**

# An electrically pumped surface-emitting semiconductor green laser

Yong-Ho Ra<sup>1,2</sup>, Roksana Tonny Rashid<sup>1</sup>, Xianhe Liu<sup>1,3</sup>, Sharif Md. Sadaf<sup>1,4</sup>, Kishwar Mashooq<sup>3</sup>, Zetian Mi<sup>1,3</sup>\*

Surface-emitting semiconductor lasers have been widely used in data communications, sensing, and recently in Face ID and augmented reality glasses. Here, we report the first achievement of an all-epitaxial, distributed Bragg reflector (DBR)–free electrically injected surface-emitting green laser by exploiting the photonic band edge modes formed in dislocation-free gallium nitride nanocrystal arrays, instead of using conventional DBRs. The device operates at ~523 nm and exhibits a threshold current of ~400 A/cm², which is over one order of magnitude lower compared to previously reported blue laser diodes. Our studies open a new paradigm for developing low-threshold surface-emitting laser diodes from the ultraviolet to the deep visible (~200 to 600 nm), wherein the device performance is no longer limited by the lack of high-quality DBRs, large lattice mismatch, and substrate availability.

Copyright © 2020 The Authors, some rights reserved; exclusive licensee American Association for the Advancement of Science. No claim to original U.S. Government Works. Distributed under a Creative Commons Attribution NonCommercial License 4.0 (CC BY-NC).

#### INTRODUCTION

Vertical-cavity surface-emitting laser (VCSEL) diodes, first presented in 1979 (1), emit a coherent optical beam vertically from the device top surface and offer a number of advantages compared to conventional edge-emitting lasers, including lower threshold (2), circular and low-divergence output beam (3), single longitudinal mode emission (4), longer lifetime (5), and easy production of dense twodimensional (2D) arrays (6-11). Commercial VCSELs are fabricated on GaAs and InP substrates (12,13), which emit light mostly in the near-infrared wavelengths (14,15). Gallium nitride (GaN)-based semiconductors are the material of choice for lasers operating in the visible and ultraviolet (UV) spectral ranges, and substantial efforts have been devoted to developing GaN-based VCSELs in the past decade (16–21). However, the operation wavelengths have been largely limited to the blue spectral range (22–25). To date, there has been no demonstration of all-epitaxial surface-emitting laser diodes operating in the green wavelength region, to which eyes are most sensitive. To the best of our knowledge, the only previously reported room temperature continuous wave (CW) surface-emitting green laser diode relied on the use of dual dielectric distributed Bragg reflectors (DBRs) and wafer bonding to a copper plate for low thermal resistance (26). The realization of a low-threshold, high-efficiency, all-epitaxial surface-emitting green laser diode will enable many exciting applications including projection displays such as pico projectors, plastic optical fiber communication, wireless communication, optical storage, smart lighting, and biosensors (27–30).

An essential component of a VCSEL is DBRs, which consist of multiple alternative layers of materials with a relatively large difference in refractive index to provide very high reflectivity. DBRs with nearly lattice matched layers can be readily formed in GaAs- and InP-based materials systems (12) but have remained a critical challenge for GaN-based materials. The large lattice mismatch between GaN and AlN (~2.5%) and between GaN and InN (~11%) (31, 32), together

<sup>1</sup>Department of Electrical and Computer Engineering, McGill University, 3480 University Street, Montreal, Quebec H3A 0E9, Canada. <sup>2</sup>Optic and Electronic Component Material Center, Korea Institute of Ceramic Engineering and Technology, Jinju, Republic of Korea. <sup>3</sup>Department of Electrical Engineering and Computer Science, University of Michigan, Ann Arbor, MI 48109, USA. <sup>4</sup>Advanced Electronics and Photonics, National Research Council Canada, Ottawa K1A 0R6, Canada. \*Corresponding author. Email: ztmi@umich.edu

with the difficulty in achieving efficient p-type conduction (33), leads to GaN-based DBRs with high electrical resistivity (34), large densities of defects and dislocations (35, 36), and relatively low reflectivity. In addition, the presence of strong polarization field and the resulting quantum-confined Stark effect (QCSE) of conventional c-plane GaN devices further reduces the rate of radiative recombination, resulting in higher threshold and instable operation (37). To address these issues, GaN-based blue VCSELs have been reported by using AlInN/GaN DBRs (22) or dual-dielectric DBRs (38) and by growing on m-plane GaN substrate (39). The resulting devices, however, still exhibit a very large threshold current density ( $J_{\rm th} > 10~{\rm kA/cm}^2$ ) at room temperature, with the operation wavelengths limited to 400 to 460 nm (22, 40).

In this work, we propose and demonstrate a nanocrystal surfaceemitting laser (NCSEL) diode, which is free of DBRs and can operate efficiently in the green spectrum. Schematically shown in Fig. 1A, the NCSEL consists of InGaN/AlGaN nanocrystal arrays with precisely controlled size, spacing, and surface morphology. Because of the efficient strain relaxation, such nanostructures are free of dislocations (41). Multiple InGaN quantum disks are incorporated on the semipolar planes of the active region, which can significantly reduce QCSE (42). A unique AlGaN shell structure (Fig. 1C) is formed surrounding the active region of the NCSEL to suppress surface recombination. By exploiting the photonic band edge resonant effect of the nanocrystal array, we have demonstrated an electrically injected surface-emitting green laser diode without using conventional thick and resistive DBRs. The device operates at 523.1 nm and exhibits a low threshold current density of ~400 A/cm<sup>2</sup> and highly stable operation at room temperature. The achievement of coherent lasing oscillation is further confirmed by the far-field emission pattern and by detailed polarization measurements. This work demonstrates a viable approach to realizing high-performance surface-emitting laser diodes from the deep UV to the deep visible (~210 to 600 nm) that were previously difficult to achieve.

### **RESULTS AND DISCUSSION**

Schematically shown in Fig. 1 (A to C) is the design of the InGaN NCSEL, which consists of an n-type GaN cladding layer (~370 nm thick), an InGaN multiple quantum disk active region, and a p-type

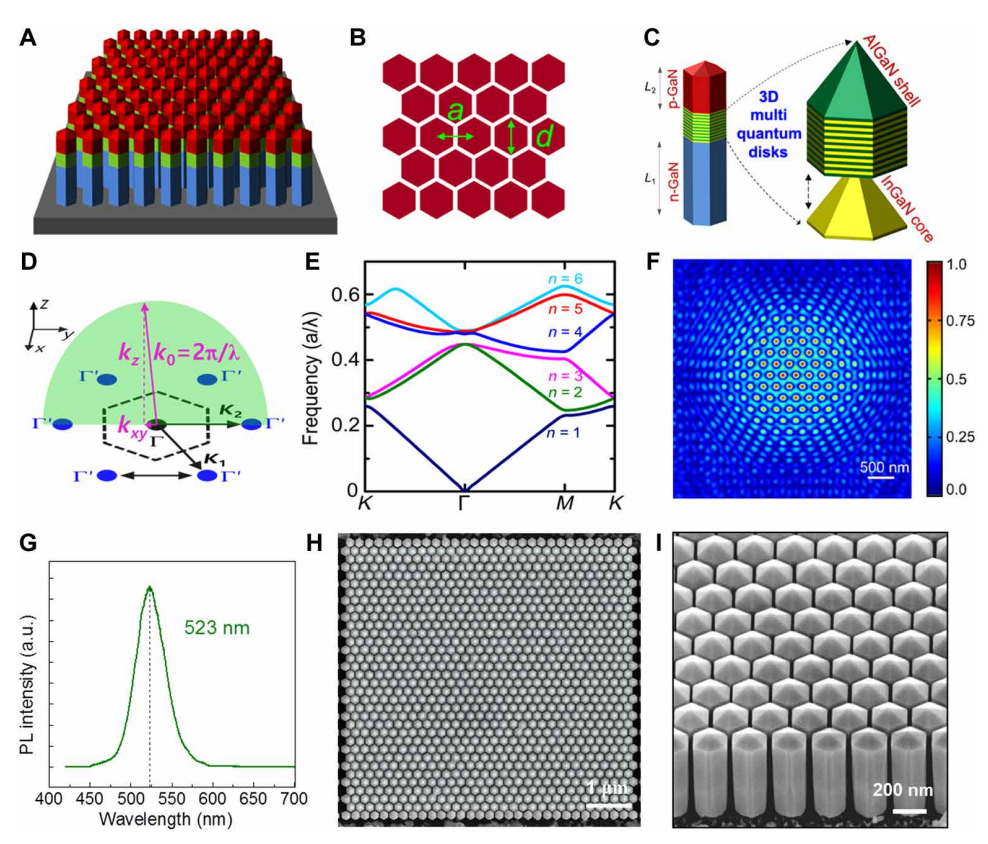


**Fig. 1. Design of InGaN NCSEL diodes operating in the green wavelength.** (**A**) Schematic of the InGaN nanocrystal arrays for the surface-emitting laser diode. (**B**) The diameter and lattice constant of the nanocrystals denoted as d and a, respectively. (**C**) Schematic of the InGaN/AlGaN nanowire heterostructure, which consists of an n-GaN cladding layer, a core-shell InGaN/AlGaN multiple quantum disk active region, and a p-GaN cladding layer. (**D**) The reciprocal lattice of a photonic crystal structure has six equivalent  $\Gamma'$  points, which are coupled together by the Bragg grating vectors  $K_1$  and  $K_2$ . (**E**) Calculated photonic band structure for transverse magnetic (TM) polarization from 2D finite-element method (2D-FEM) simulation. (**F**) The electric field profile of the band edge mode ( $\lambda$  = 523 nm) calculated by the 3D finite-difference time-domain method. (**G**) PL spectrum of an InGaN/AlGaN calibration sample showing spontaneous green emission. a.u., arbitrary units. (**H** and **I**) The top-view and titled-view scanning electron microscopy (SEM) images of an InGaN nanocrystal array.

GaN cladding layer (190 nm thick). The nanocrystals have a hexagonal shape and are arranged in a triangular lattice. The diameter and lattice constant of the nanocrystals are denoted as d and a, respectively (Fig. 1B). The design and simulation, including energy band diagram and mode profile, were performed using 2D finite-element method (2D-FEM) simulation with Maxwell's equations (see Materials and Methods, fig. S1, and text S1). Shown in Fig. 1D, the reciprocal lattice of a photonic crystal structure has six equivalent  $\Gamma'$  points, which are coupled together by the Bragg grating vectors, e.g.,  $K_1$  and  $K_2$ . The corresponding wavelength light can therefore form a standing wave resonant in the photonic crystal without any additional dielectric mirror (43, 44). Besides such in-plane coupling, there is also out-of-plane coupling between the six  $\Gamma'$  points and the  $\Gamma$  point, which has zero in-plane wave vector (45). The wave vector is essentially vertical, thereby leading to surface emission (Fig. 1D). In this design, the nanocrystals have a spacing of ~30 nm, and the lattice constant is 250 nm.

The resulting photonic band structure for transverse magnetic (TM) polarization ( $E \parallel c$  axis) from 2D-FEM simulation is shown in Fig. 1E. The  $\Gamma$  point in the fourth band is located at ~0.48 a/ $\lambda$ , which corresponds to  $\lambda$  ~ 520 nm. The group velocity is determined by the slope of the dispersion curve in the photonic band structure. At the band edge, the low group velocity is achieved when the slope of the dispersion curve becomes zero; i.e., near the  $\Gamma$  point, the group

velocity of light becomes zero  $(dw/dk \rightarrow 0)$ , thereby leading to the formation of a stable and large single-cavity mode (46-50). The mode profile is simulated and shown in Fig. 1F. The mode intensity is mostly distributed in the nanocrystals. The extremely low group velocity leads to the long interaction time between radiation field and active material and consequently gives rise to a strong gain enhancement. Photons are also confined around the active region in the vertical direction, due to the higher average refractive index in the active region. The mode intensity profile in the vertical direction is shown in fig. S1. The simulation details are described in text S1.

The realization of NCSELs requires a precise control of the nanocrystal size, spacing, and uniformity across a relatively large area. The fabrication of such nanocrystal arrays is achieved by the special technique of selective area epitaxy using plasma-assisted molecular beam epitaxy (MBE) (see Materials and Methods, fig. S2, and text S2) (51, 52). An AlGaN shell structure was incorporated in the active region to reduce surface recombination (53, 54). Figure 1G shows the photoluminescence (PL) spectrum for a calibration sample without significant photonic band edge resonant effect. The peak emission wavelength is ~523 nm. Significantly enhanced PL emission intensity was measured for the InGaN/AlGaN core-shell structure, compared to similar structures but without AlGaN shell (fig. S6 and texts S3 and S7). Shown in Fig. 1 (H and I) are the top-view and titled-view scanning electron microscopy (SEM) images of the InGaN nanocrystals

for a 6  $\mu$ m by 6  $\mu$ m area. The nanocrystal arrays have a triangular lattice with a pitch of 250 nm, a lateral size of 230 nm, a height of ~600 nm, and a gap between neighboring nanocrystals of ~30 nm. The nanocrystals exhibit uniform length, smooth sidewalls, and near-perfect hexagonal shape and high (depth-to-width) aspect ratio, which correlate well with the design parameters described above.

We further performed detailed structural characterization of InGaN nanocrystals using scanning transmission electron microscopy (STEM) (see Materials and Methods, fig. S3, and text S4). We prepared a cross-sectional sample using a focused ion beam system. Figure 2A shows the high-angle annular dark-field (HAADF) atomic number contrast image of a representative InGaN nanocrystal. The InGaN/AlGaN heterostructures were formed as a cone shape. This is due to the formation of n-GaN nanocrystals that have a Ga polarity and pyramid-like morphology (fig. S4 and text S5). The resulting unique structure takes advantage of the semipolar effect in the active region to reduce the polarization field in GaN wurtzite structure (55). Shown in Fig. 2B is a high-magnification image taken from the marked region in Fig. 2A. The sloping multiple quantum disk layers can be more clearly observed. The formation of multiple quantum disk heterostructures on semipolar planes of (0113) orientation is further supported by the representative selected-area electron diffraction pattern analysis (Fig. 2C).

From the wide-thickness layers with the bright contrast in the middle region, it can be seen that multiple quantum disk structures are formed as a cone-like shell structure (Fig. 2C, fig. S5, and text S6). The formation of this cone-shaped active layer is further supported by the formation of the n-GaN structure as shown in text S6.

The unique 3D structure provides an emission area that is much larger than that of the typical quantum disk/dot active regions aligned vertically with the same diameter. Figure 2D shows the highmagnification HAADF image of the InGaN/AlGaN active region. The presence of highly uniform multiple quantum disk layers can be identified by different contrast. No noticeable extended misfit dislocations or stacking faults were observed. The thicknesses of the InGaN disks and AlGaN barriers are ~2.5 and 1.5 nm, respectively. To further confirm elemental distribution of the active region, we performed an energy-dispersive x-ray spectrometry (EDXS) analysis along the growth direction of InGaN/AlGaN quantum disks, which is labeled with "1" in Fig. 2D. The qualitative variations of In and Al across different disks and barriers are shown in Fig. 2E. Because the atomic number of Al is smaller than the atomic number of In, it appears as dark contrast in the STEM image. The In signal exhibits a maximum in the bright regions and drops in the dark regions. In contrast, the Al signal shows clear peaks in the dark regions, confirming the formation of InGaN/AlGaN quantum disk heterostructures. The presence of an Al-rich AlGaN shell layer formed spontaneously on the sidewall of the InGaN quantum disk is also confirmed by the EDXS point analysis (Fig. 2F). The spontaneously formed AlGaN shell structure can effectively suppress nonradiative surface recombination, a primary limiting factor for the performance of conventional nanostructured devices (54). Moreover, the semipolar InGaN/AlGaN core-shell heterostructure further offers several distinct advantages, including significantly reduced polarization fields (42) and enhanced light emission efficiency (56), as well as significantly improved carrier injection efficiency (53) and

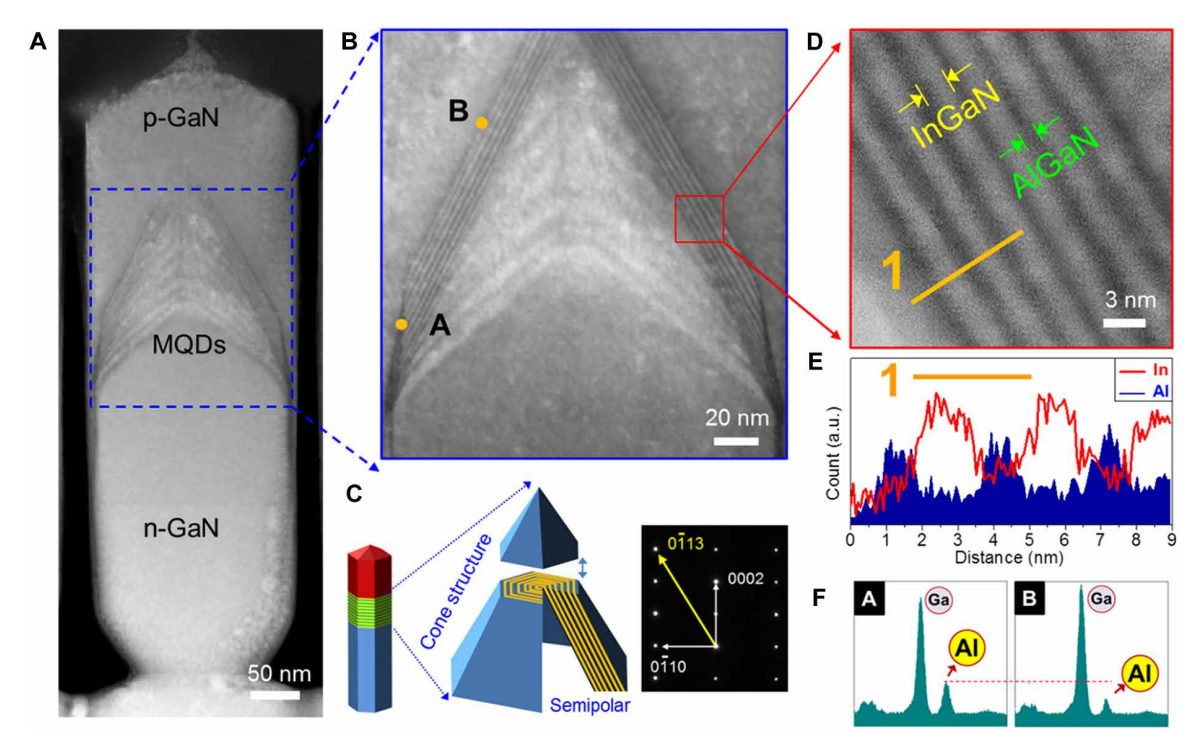


Fig. 2. Structural characterization of InGaN/AlGaN core-shell quantum disk heterostructures. (A) STEM-HAADF image of a representative core-shell InGaN/AlGaN multiple quantum disk (MQD) heterostructure nanocrystal. (B) High-magnification image taken from the region marked in (A) and (C) schematic illustration for the quasi-3D structure of the semipolar active region and selected-area electron diffraction pattern of the InGaN/AlGaN core-shell heterostructure. (D) High-magnification HAADF image of the InGaN/AlGaN quantum disk region. (E) Energy-dispersive x-ray spectroscopy (EDXS) line profile of the InGaN/AlGaN quantum disks along the line labeled with "1" in (D). (F) EDXS point analysis of the AlGaN shell region marked as "A" and "B" in (B).

luminescence efficiency (57), compared to conventional quantum disk/dot structures (fig. S6 and text S7). It is also worthwhile to mention that such a unique structure cannot be fabricated by the conventional top-down approach because the active region is predefined by the film structure.

We fabricated InGaN NCSEL diodes using planarization, polyimide passivation, contact metallization, and photolithography techniques (fig. S7 and text S8). Schematic illustration of the fabricated device is shown in Fig. 3A, and an optical microscopy image of the device after metallic contact grids is also shown in the inset. Shown in Fig. 3B is a representative current-voltage (*I-V*) curve for a device with surface contact area of ~25  $\mu m^2$ , which shows rectification characteristics with a sharp turn-on voltage of ~3.3 V at room temperature. The leakage current is negligible under reverse bias (Fig. 3B, inset). The device exhibited excellent *I-V* characteristics, which is partly due to the significantly reduced defect density and enhanced dopant incorporation in nanocrystal structures (58, 59). The electroluminescence characteristics were measured under CW biasing conditions at room temperature. We collected the emitted light from the top surface of the nanocrystal (fig. S8 and text S9).

Figure 3C shows the electroluminescence spectra of the nanocrystal device measured under different injection currents. At a low injection current density of  $\sim\!200~\text{A/cm}^2$ , the device exhibits a broad emission spectrum centered at  $\sim\!524~\text{nm}$ , with a full width at half maximum (FWHM) of  $\sim\!30~\text{nm}$ , which corresponds to the spontaneous emission and may be limited by nonuniform current injection. We observed a sharp lasing peak at  $\sim\!523.1\text{-nm}$  wavelength with increasing injection current, with a narrow linewidth of  $\sim\!0.8~\text{nm}$ . The strong lasing

spot is shown in the inset of Fig. 3A, which was recorded at a current density of  $\sim\!1$  kA/cm². We further measured variations of the output power versus injection current, which exhibits a clear threshold at  $\sim\!400$  A/cm² (Fig. 3D). The measured lasing threshold is significantly lower compared to previously reported GaN VCSELs (22, 26, 27, 40, 60, 61). An output power of  $\sim\!12~\mu\mathrm{W}$  was measured at an injection current density of  $\sim\!1$  kA/cm² under CW operation. The output power shows saturation with further increasing the injection current, due to the heating effect. The measured output power is significantly higher than previously reported values of GaN-based VCSELs operating at 460 and 500 nm (62) and can be further improved by optimizing the design and fabrication process.

Variations of spectral linewidth (FWHM) and wavelength peak position are investigated under different injection current densities (Fig. 3, E and F). The spectral linewidth was decreased from ~30 to 0.8 nm at the threshold. It is also seen that the lasing peak position remains nearly constant at ~523 nm above threshold, suggesting highly stable lasing of the core-shell nanocrystal lasers. The low-threshold current density and highly stable emission are directly related to the robust photonic band edge mode of nanocrystal optical cavity, the dislocation-free bottom-up nanocrystal structure, and the reduced nonradiative surface recombination and suppressed polarization field with the extended emission area in the InGaN/AlGaN cone-like shell active region.

The far-field radiation pattern of the nanocrystal laser structure was simulated using the 3D finite-difference time-domain (FDTD) method, shown in Fig. 4A (see Materials and Methods and text S10). Because the wavelength near the  $\Gamma$  point has a very small in-plane

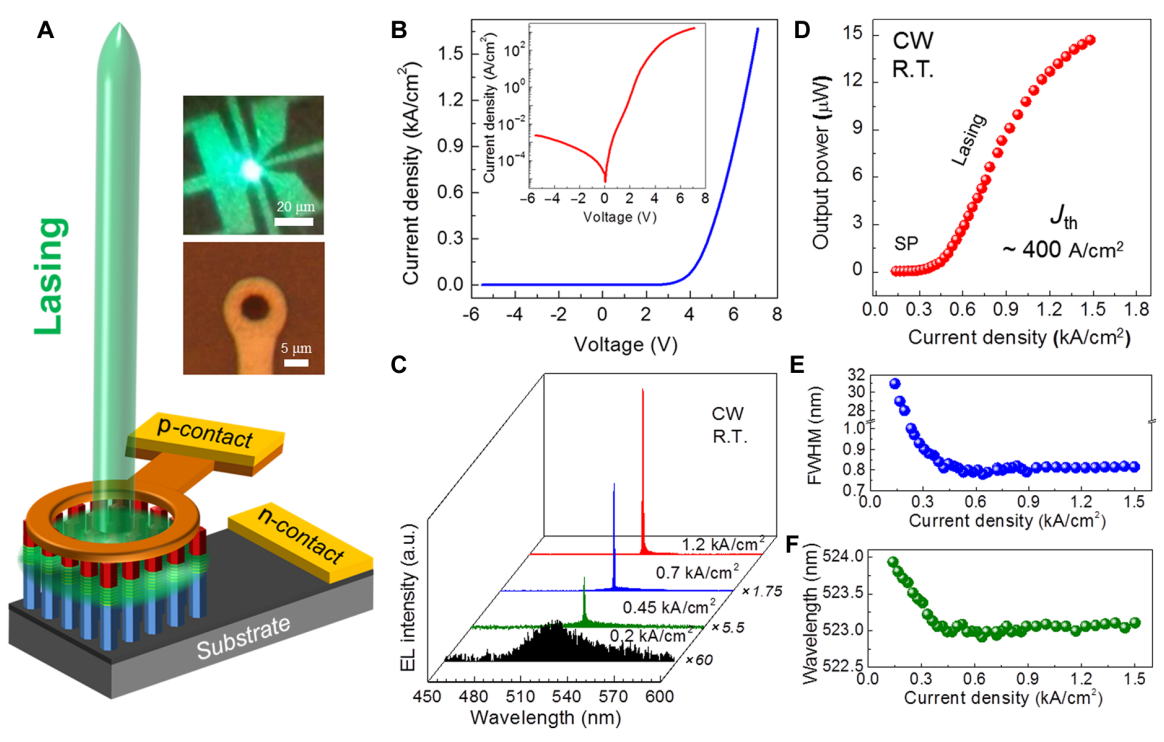
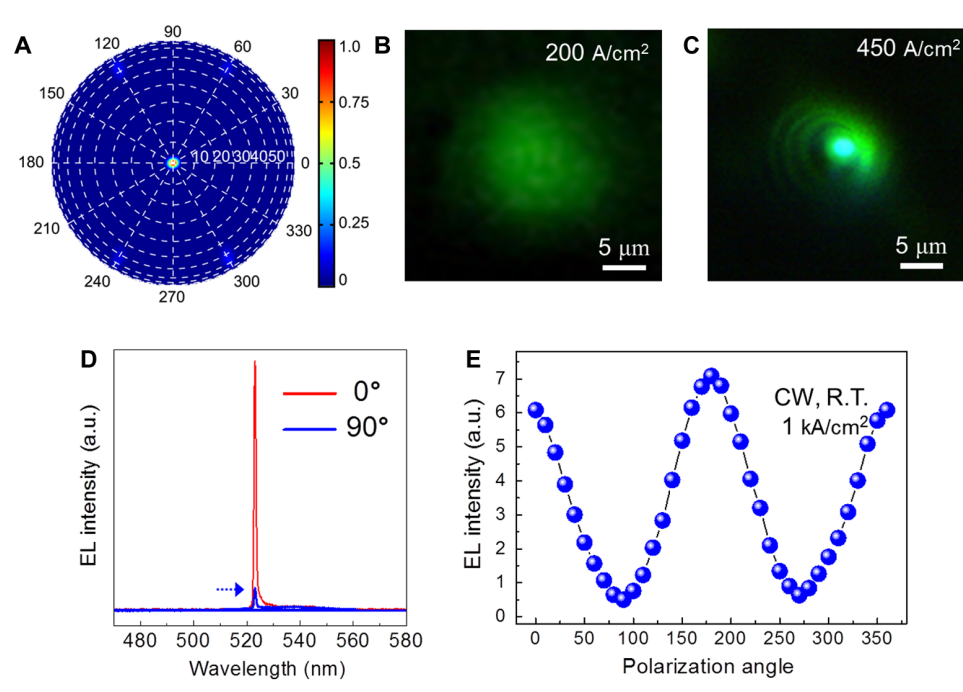


Fig. 3. Fabrication and characterization of InGaN NCSEL diodes. (A) Schematic illustration of the fabricated NCSEL device. Inset: Optical microscopy image of the device after metallic contact grids and electroluminescence (EL) image of the green lasing. (B) Current-voltage (*I-V*) characteristics of the NCSEL device. Inset: The *I-V* curve on a semi-log scale. (C) Electroluminescence spectra measured from different injection currents under CW biasing conditions at room temperature (R.T.). (D) Variations of the output power versus injection current. It shows a clear threshold of ~400 A/cm<sup>2</sup>. SP, spontaneous emission. (E) Variations of spectral linewidth (FWHM, full width at half maximum). (F) Peak wavelength position measured under different injection current densities.



**Fig. 4. Far-field and polarization emission properties of InGaN NCSEL diodes.** (**A**) Far-field radiation pattern of the nanocrystal laser structure simulated using the 3D FDTD method. Electroluminescence image of the far-field pattern observed below the threshold current density (200 A/cm²) (**B**) and slightly above the threshold current density (**C**) of the InGaN NCSEL recorded using a high-resolution charge-coupled device (CCD) camera above the device top surface. (**D**) Polarized electroluminescence spectra of the InGaN NCSEL measured under a current density of 1 kA/cm². The polarization ratio is ~0.86. (**E**) The measured electroluminescence intensity as a function of the emission polarization angle (0° to 360°).

wave vector component, the wave vector is expected to be almost vertical. Because of this unique property of the  $\Gamma$  point, the far-field pattern exhibits a spot in the center with a very small divergence angle, which corresponds to highly collimated vertical emission. The far-field patterns measured below and above threshold of the InGaN NCSEL are shown in Fig. 4 (B and C), respectively (fig. S9 and text S11). Below threshold, the far-field image shows emission without any interference fringes, with the uniformity partly limited by the current spreading and injection at relatively low current densities. When the current density is above threshold, the lasing emission shows the presence of interference fringes that indicate coherent emission (63–67). Such results provide strong evidence that the coherent lasing oscillation has been achieved in InGaN nanocrystal arrays.

We have further studied the polarization properties in the far-field light emission of InGaN NCSELs (see Materials and Methods). The degree of polarization is defined as  $\rho = (I_{0^{\circ}} - I_{90^{\circ}})/(I_{0^{\circ}} + I_{90^{\circ}})$  (fig. S10 and text S12), where  $I_{0^{\circ}}$  and  $I_{90^{\circ}}$  are the electroluminescence emission intensity, corresponding to the electric field along the 0° and 90° direction, respectively. Figure 4D shows the electroluminescence spectra measured under a current density of 1 kA/cm<sup>2</sup> for different polarizations. It is seen that the electroluminescence emission is highly polarized. The degree of polarization is as large as 0.86. Variations of electroluminescence intensity versus polarization angle  $(\theta)$  are further plotted in Fig. 4E, showing a high degree of polarization at  $\theta = 0^{\circ}$ . It is worthwhile to mention that this is a remarkably stable and directional polarized emission compared to conventional photonic crystal laser devices (45, 68). These studies also provide unambiguous evidence for the achievement of a surface-emitting laser.

#### **CONCLUSIONS**

A new generation of surface-emitting laser diodes using bottom-up InGaN nanocrystals has been demonstrated. The presence of a clear threshold, sharp linewidth reduction, distinct far-field emission pattern, and polarized light emission provides unambiguous evidence for the achievement of coherent lasing oscillation. Significantly, compared to the conventional GaN VCSELs, lasing and surface emission are achieved without using thick, resistive, and often heavily dislocated DBRs. This unique laser concept can be readily extended to achieve all-epitaxial, DBR-free surface-emitting laser diodes operating across the entire visible, as well as mid and deep UV wavelengths, and to realize such lasers on low-cost, large-area Si wafers. Our studies therefore open a new paradigm in the design and development of surface-emitting laser diodes, wherein the performance is no longer limited by the availability of DBRs, lattice mismatch, and substrate availability.

# **MATERIALS AND METHODS**

#### InGaN NCSEL design and simulation

The band structure for nanocrystal arrays with a triangular lattice was firstly calculated by 2D-FEM simulation using the radio frequency (RF) module in the commercial software package COMSOL Multiphysics 4.3b. The refractive index of nanocrystals was assumed to be 2.56. The filling material (polyimide) between the nanocrystals has a refractive index of 1.75. The simulation was performed for a unit cell with Floquet periodic boundary condition to solve for different points in the k space. The lattice constant and nanocrystal diameter were subsequently varied to tune the  $\Gamma$  point of the fourth band to be ~520 nm. Then, the same lattice constant and nanocrystal

diameter were used to simulate a nanocrystal array with dimensions of about 5  $\mu m$  by 5  $\mu m$ . The in-plane mode profile was also calculated by 2D-FEM simulation. The boundary conditions were impedance boundary conditions with a refractive index of 1.75, which is the same as the filling material. Possible modes around the  $\Gamma$  point of the fourth band were computed, and the one exhibiting profile that is characteristic of the  $\Gamma$  point was identified.

#### **MBE** growth

The nanocrystal arrays were grown on an n-type GaN template on a sapphire substrate by the RF plasma-assisted MBE (Veeco GENxplor) system. n-GaN:Si nanocrystal arrays were first grown with a substrate temperature of 850°C, a nitrogen flow rate of 0.4 standard cubic centimeters per minute (sccm), and a Ga beam equivalent pressure (BEP) of ~2.9  $\times$  10 $^{-7}$  torr. The growth conditions for the vertically aligned InGaN/AlGaN quantum disk active region included a substrate temperature of 650°C, a nitrogen flow rate of 1.2 sccm, a Ga BEP in the range of 1.8  $\times$  10 $^{-8}$  torr, an In BEP of approximately 8.1  $\times$  10 $^{-8}$  torr, and an Al BEP in the range of 4.2  $\times$  10 $^{-9}$  torr, respectively. For the top p-GaN:Mg nanocrystals, Mg cell temperatures of 330°C were used with a Mg BEP of ~ 1.5  $\times$  10 $^{-9}$  torr and a nitrogen flow rate of 0.6 sccm. A forward plasma power of ~350 W was used during the full structure growth.

#### Optical and structural characterization

PL measurement was carried out using a 405-nm laser as the excitation source with a visible neutral density filter. The optical emission was spectrally resolved using a high-resolution iHR550 imaging spectrometer and detected by a high-sensitivity liquid nitrogen–cooled charge-coupled device (CCD). SEM images were taken using a FEI Inspect F50 FE-SEM system. The measurements were performed with a 90° (top view) and a 45° tilted angle from the cross section of the sample. An accelerating voltage of 10 kV was used for imaging. STEM measurement was performed using a JEOL JEM-2100F equipped with a field-emission gun with an accelerating voltage of 200 kV. STEM-HAADF imaging was measured with an electron beam diameter of approximately 0.1 nm. A silicon drift detector of a 60 mm² was used for STEM-EDXS analysis.

#### Laser device fabrication

The NCSEL devices were fabricated by the following steps. The nanocrystal arrays were first planarized by a spin-coating system using a polyimide layer, followed by O<sub>2</sub> plasma etching to expose the top surface of the nanocrystals. A SiO<sub>x</sub> passivation layer (~50 nm thick) was further deposited by plasma-enhanced chemical vapor deposition at 300°C, and the device active region area is defined by the opening aperture on the  $SiO_x$  layer. A metal electrode consisting of Ni (8 nm)/Au (8 nm) was deposited on the p-GaN top surface by an e-beam evaporator with an e-beam lithography technique and then annealed at  $\sim$ 550°C for 2 min in N<sub>2</sub> gas ambient. Subsequently, an 80-nm-thick indium tin oxide (ITO) layer was deposited to serve as a transparent electrode and current spreading layer. The ITO contact was also annealed at 300°C for 1 hour in vacuum. Ni (20 nm)/Au (100 nm) and Ti (20 nm)/Au (100 nm) contact layers were deposited on the surrounding ITO top surface and n-GaN template to serve as the p- and n-metal contacts, respectively. The fabricated devices with metal contacts were annealed at ~550°C for 2 min in N<sub>2</sub> gas ambient.

#### Laser device characterization

For electrical injection measurements, the InGaN device was placed on a motorized *x-y* stage (Aerotech's ANT130-XYULTRA), which provided precise spatial mapping. The current-voltage characteristics of the device were performed by a source meter Keithley SMU-2400. The output power was measured using a Si photodiode sensor. Electroluminescence spectra were measured by a liquid nitrogen—cooled CCD attached to an iHR550 spectrometer with 1200 grooves/mm grating. The far-field images were captured by a high megapixel color CCD camera at a distance above the top surface of the device. The polarization was resolved by a Glan-Taylor calcite polarizer (with a High-Precision Rotation Mount) installed on the top surface of the device.

#### SUPPLEMENTARY MATERIALS

Supplementary material for this article is available at http://advances.sciencemag.org/cgi/content/full/6/1/eaav7523/DC1

Text S1. Simulation for photon confinement in the vertical direction

Text S2. Nanohole patterned Ti mask substrate for selective area epitaxy

Text S3. Epitaxial growth of InGaN/AlGaN core-shell heterostructures

Text S4. TEM specimen preparation using a focused ion beam system

Text S5. Ga-polar n-GaN nanocrystal structure

Text S6. Projection effect image and quasi-3D structure of InGaN/AlGaN quantum disk layers

Text S7. Properties of semipolar InGaN/AlGaN core-shell heterostructures

Text S8. NCSEL device fabrication

Text S9. Electroluminescence measurement

Text S10. Calculation of far-field radiation pattern

Text S11. Measurement of far-field radiation pattern

Text S12. Polarization measurement of the light emission of InGaN NCSELs

Fig. S1. Variation of the effective refractive index along the growth direction and the TM polarized mode intensity profile.

Fig. S2. Schematic illustration and field-emission SEM image of the patterned Ti thin-film nanohole mask fabricated on n-type GaN template substrate.

Fig. S3. TEM lamella preparation of the nanocrystal.

Fig. S4. Ga-polar n-GaN nanocrystal structure.

Fig. S5. Projection effect in quasi-3D structure.

Fig. S6. PL emission spectra of InGaN/AlGaN core-shell multiquantum disk nanocrystals (green curve) and InGaN/GaN multiquantum disk nanocrystals without AlGaN shell (blue curve) measured at 300 K.

Fig. S7. Schematic illustration of the full device fabrication, including passivation, planarization, photolithography, and contact metallization techniques.

Fig. S8. Schematic illustration of the measurement setup for electroluminescence spectra. Fig. S9. Schematic illustration of the far-field measurement setup with a CCD camera at a distance above the NCSEL device.

Fig. S10. Schematic illustration of the polarization angle measurement. References (69–83)

### REFERENCES AND NOTES

- H. Soda, K.-i. Iga, C. Kitahara, Y. Suematsu, GalnAsP/InP surface emitting injection lasers. Jpn. J. Appl. Phys. 18, 2329–2330 (1979).
- D. G. Deppe, D. L. Huffaker, O. Tchang-Hun, D. Hongyu, D. Qing, Low-threshold vertical-cavity surface-emitting lasers based on oxide-confinement and high contrast distributed Bragg reflectors. *IEEE J. Sel. Top. Quantum Electron.* 3, 893–904 (1997).
- A. M. Kasten, D. F. Siriani, M. K. Hibbs-Brenner, K. L. Johnson, K. D. Choquette, Beam properties of visible proton-implanted photonic crystal VCSELs. *IEEE J. Sel. Top. Quantum Electron.* 17, 1648–1655 (2011).
- J. P. Tourrenc, S. Bouchoule, A. Khadour, J. Decobert, A. Miard, J. C. Harmand, J. L. Oudar, High power single-longitudinal-mode OP-VECSEL at 1.55 

  μm with hybrid metalmetamorphic Bragg mirror. Electron. Lett. 43, 754–755 (2007).
- P. Westbergh, J. S. Gustavsson, B. Kögel, A. Haglund, A. Larsson, Impact of photon lifetime on high-speed VCSEL performance. *IEEE J. Sel. Top. Quantum Electron.* 17, 1603–1613 (2011).
- K. Iga, Surface-emitting laser—Its birth and generation of new optoelectronics field. IEEE J. Sel. Top. Quantum Electron. 6, 1201–1215 (2000).
- F. H. Peters, M. G. Peters, D. B. Young, J. W. Scott, B. J. Thibeault, S. W. Corzine, L. A. Coldren, High-power vertical-cavity surface-emitting lasers. *Electron. Lett.* 29, 200–201 (1993).

# SCIENCE ADVANCES | RESEARCH ARTICLE

- D. Francis, W. Yuen, H.-L. Chen, G. Li, C. Chang-Hasnain, Monolithic 2D-VCSEL array with >2 W CW and >5 W pulsed output power. *Electron. Lett.* 34, 2132–2133 (1998).
- D. Bimberg, N. N. Ledentsov, M. Grundmann, N. Kirstaedter, O. G. Schmidt, M. H. Mao, V. M. Ustinov, A. Y. Egorov, A. E. Zhukov, P. S. Kopev, Z. I. Alferov, S. S. Ruvimov, U. Gösele, J. Heydenreich, InAs-GaAs quantum dots: From growth to lasers. *Phys. Status Solidi B* 194, 159–173 (1996).
- Y. Arakawa, H. Sakaki, Multidimensional quantum well laser and temperature dependence of its threshold current. Appl. Phys. Lett. 40, 939–941 (1982).
- E. Yablonovitch, Inhibited spontaneous emission in solid-state physics and electronics. *Phys. Rev. Lett.* 58, 2059–2062 (1987).
- F. Koyama, S. Kinoshita, K. Iga, Room-temperature continuous wave lasing characteristics of a GaAs vertical cavity surface-emitting laser. Appl. Phys. Lett. 55, 221–222 (1989).
- M.-C. Amann, W. Hofmann, InP-based long-wavelength VCSELs and VCSEL arrays. IEEE J. Sel. Top. Quantum Electron. 15, 861–868 (2009).
- C. Gierl, T. Gruendl, P. Debernardi, K. Zogal, C. Grasse, H. A. Davani, G. Böhm, S. Jatta, F. Küppers, P. Meißner, M.-C. Amann, Surface micromachined tunable 1.55 μm-VCSEL with 102 nm continuous single-mode tuning. Opt. Express 19, 17336–17343 (2011).
- D. Saxena, S. Mokkapati, P. Parkinson, N. Jiang, Q. Gao, H. H. Tan, C. Jagadish, Optically pumped room-temperature GaAs nanowire lasers. Nat. Photonics 7, 963–968 (2013).
- M. A. Khan, D. T. Olson, J. M. Van Hove, J. N. Kuznia, Vertical-cavity, room-temperature stimulated emission from photopumped GaN films deposited over sapphire substrates using low-pressure metalorganic chemical vapor deposition. *Appl. Phys. Lett.* 58, 1515–1517 (1991).
- J. M. Redwing, D. A. S. Loeber, N. G. Anderson, M. A. Tischler, J. S. Flynn, An optically pumped GaN-AlGaN vertical cavity surface emitting laser. Appl. Phys. Lett. 69, 1–3 (1996).
- H. Zhou, M. Diagne, E. Makarona, A. V. Nurmikko, J. Han, K. E. Waldrip, J. J. Figiel, Near ultraviolet optically pumped vertical cavity laser. *Electron. Lett.* 36, 1777–1779 (2000).
- C.-C. Kao, Y. C. Peng, H. H. Yao, J. Y. Tsai, Y. H. Chang, J. T. Chu, H. W. Huang, T. T. Kao, T. C. Lu, H. C. Kuo, S. C. Wang, C. F. Lin, Fabrication and performance of blue GaN-based vertical-cavity surface emitting laser employing AlN/GaN and Ta<sub>2</sub>O<sub>5</sub>/SiO<sub>2</sub> distributed Bragg reflector. *Appl. Phys. Lett.* 87, 081105 (2005).
- S.-H. Park, J. Kim, H. Jeon, T. Sakong, S.-N. Lee, S. Chae, Y. Park, C.-H. Jeong, G.-Y. Yeom, Y.-H. Cho, Room-temperature GaN vertical-cavity surface-emitting laser operation in an extended cavity scheme. *Appl. Phys. Lett.* 83, 2121–2123 (2003).
- T. Tawara, H. Gotoh, T. Akasaka, N. Kobayashi, T. Saitoh, Low-threshold lasing of InGaN vertical-cavity surface-emitting lasers with dielectric distributed Bragg reflectors. *Appl. Phys. Lett.* 83, 830–832 (2003).
- G. Cosendey, A. Castiglia, G. Rossbach, J.-F. Carlin, N. Grandjean, Blue monolithic AllnN-based vertical cavity surface emitting laser diode on free-standing GaN substrate. Appl. Phys. Lett. 101, 151113 (2012).
- T.-C. Lu, C.-C. Kao, H.-C. Kuo, G.-S. Huang, S.-C. Wang, CW lasing of current injection blue GaN-based vertical cavity surface emitting laser. Appl. Phys. Lett. 92, 141102 (2008).
- S. Gwo, C.-K. Shih, Semiconductor plasmonic nanolasers: Current status and perspectives. Rep. Proa. Phys. 79, 086501 (2016).
- Y. Sun, K. Zhou, Q. Sun, J. Liu, M. Feng, Z. Li, Y. Zhou, L. Zhang, D. Li, S. Zhang, M. Ikeda, S. Liu, H. Yang, Room-temperature continuous-wave electrically injected InGaN-based laser directly grown on Si. *Nat. Photonics* 10, 595–599 (2016).
- Y. Mei, G.-E. Weng, B.-P. Zhang, J.-P. Liu, W. Hofmann, L.-Y. Ying, J.-Y. Zhang, Z.-C. Li, H. Yang, H.-C. Kuo, Quantum dot vertical-cavity surface-emitting lasers covering the 'green gap'. *Light Sci. Appl.* 6, e16199 (2017).
- J. B. Wright, S. Liu, G. T. Wang, Q. Li, A. Benz, D. D. Koleske, P. Lu, H. Xu, L. Lester, T. S. Luk, I. Brener, G. Subramania, Multi-colour nanowire photonic crystal laser pixels. Sci. Rep. 3, 2982 (2013).
- M. Lu, S. S. Choi, U. Irfan, B. T. Cunningham, Plastic distributed feedback laser biosensor. Appl. Phys. Lett. 93, 111113 (2008).
- A. Unger, M. Küster, B. Köhler, J. Biesenbach, High-power fiber-coupled 100W visible spectrum diode lasers for display applications, in *Proceedings of SPIE, High-Power Diode Laser Technology and Applications XI* (26 Febuary 2013), vol. 8605, pp. 86050K.
- O. Kumagai, M. Ikeda, M. Yamamoto, Application of laser diodes to optical disk systems: The history of laser diode development and mass production in three generations of optical disk systems. *Proc. IEEE* 101, 2243–2254 (2013).
- 31. L. Liu, J. H. Edgar, Substrates for gallium nitride epitaxy. *Mater. Sci. Eng. R* **37**, 61–127 (2002)
- 32. T. Lei, K. F. Ludwig Jr., T. D. Moustakas, Heteroepitaxy, polymorphism, and faulting in GaN thin films on silicon and sapphire substrates. *J. Appl. Phys.* **74**, 4430–4437 (1993).
- J. Xie, X. Ni, Q. Fan, R. Shimada, Ü. Özgür, H. Morkoς, On the efficiency droop in InGaN multiple quantum well blue light emitting diodes and its reduction with p-doped quantum well barriers. Appl. Phys. Lett. 93, 121107 (2008).
- R. F. Kopf, E. F. Schubert, S. W. Downey, A. B. Emerson, N- and P-type dopant profiles in distributed Bragg reflector structures and their effect on resistance. *Appl. Phys. Lett.* 61, 1820–1822 (1992).

- B. Monemar, B. E. Sernelius, Defect related issues in the "current roll-off" in InGaN based light emitting diodes. Appl. Phys. Lett. 91, 181103 (2007).
- S. A. Fortuna, X. Li, Metal-catalyzed semiconductor nanowires: A review on the control of growth directions. Semicond. Sci. Technol. 25, 024005 (2010).
- C.-F. Huang, C.-Y. Chen, C.-F. Lu, C. C. Yang, Reduced injection current induced blueshift in an In Ga N/Ga N quantum-well light-emitting diode of prestrained growth. *Appl. Phys. Lett.* 91, 051121 (2007).
- L. Tien-Chang, J.-R. Chen, S.-W. Chen, H.-C. Kuo, C.-C. Kuo, C.-C. Lee, S.-C. Wang, Development of GaN-based vertical-cavity surface-emitting lasers. *IEEE J. Sel. Top. Quantum Electron.* 15, 850–860 (2009).
- C. Holder, J. S. Speck, S. P. DenBaars, S. Nakamura, D. Feezell, Demonstration of nonpolar GaN-based vertical-cavity surface-emitting lasers. *Appl. Phys. Exp.* 5, 092104 (2012).
- H. Matsubara, S. Yoshimoto, H. Saito, Y. Jianglin, Y. Tanaka, S. Noda, GaN photonic-crystal surface-emitting laser at blue-violet wavelengths. Science 319, 445–447 (2008).
- S. D. Hersee, A. K. Rishinaramangalam, M. N. Fairchild, L. Zhang, P. Varangis, Threading defect elimination in GaN nanowires. J. Mater. Res. 26, 2293–2298 (2011).
- D. F. Feezell, J. S. Speck, S. P. DenBaars, S. Nakamura, S. Semipolar, Semipolar (2021) InGaN/GaN light-emitting diodes for high-efficiency solid-state lighting. *J. Disp. Technol.* 9, 190–198 (2013).
- M. Notomi, H. Suzuki, T. Tamamura, Directional lasing oscillation of two-dimensional organic photonic crystal lasers at several photonic band gaps. *Appl. Phys. Lett.* 78, 1325–1327 (2001).
- H.-Y. Ryu, S.-H. Kwon, Y.-J. Lee, Y.-H. Lee, J.-S. Kim, Very-low-threshold photonic band-edge lasers from free-standing triangular photonic crystal slabs. *Appl. Phys. Lett.* 80, 3476–3478 (2002).
- M. Imada, A. Chutinan, S. Noda, M. Mochizuki, Multidirectionally distributed feedback photonic crystal lasers. *Phys. Rev. B* 65, 195306 (2002).
- K. Hirose, Y. Liang, Y. Kurosaka, A. Watanabe, T. Sugiyama, S. Noda, Watt-class high-power, high-beam-quality photonic-crystal lasers. *Nat. Photonics* 8, 406–411 (2014).
- F. Raineri, A. M. Yacomotti, T. J. Karle, R. Hostein, R. Braive, A. Beveratos, I. Sagnes, R. Raj, Dynamics of band-edge photonic crystal lasers. Opt. Express 17, 3165–3172 (2009).
- G. Vecchi, F. Raineri, I. Sagnes, A. Yacomotti, P. Monnier, T. J. Karle, K.-H. Lee, R. Braive, L. Le Gratiet, S. Guilet, G. Beaudoin, A. Taneau, S. Bouchoule, A. Levenson, R. Raj, Continuous-wave operation of photonic band-edge laser near 1.55 μm on silicon wafer. Opt. Express 15, 7551–7556 (2007).
- D. Zhao, S. Liu, H. Yang, Z. Ma, C. Reuterskiöld-Hedlund, M. Hammar, W. Zhou, Printed large-area single-mode photonic crystal bandedge surface-emitting lasers on silicon. *Sci. Rep.* 6, 18860 (2016).
- V. Reboud, J. Romero-Vivas, P. Lovera, N. Kehagias, T. Kehoe, G. Redmond, C. M. Sotomayor Torres, Lasing in nanoimprinted two-dimensional photonic crystal band-edge lasers. *Appl. Phys. Lett.* **102**, 073101 (2013).
- B. H. Le, S. Zhao, X. Liu, S. Y. Woo, G. A. Botton, Z. Mi, Controlled coalescence of AlGaN nanowire arrays: An architecture for nearly dislocation-free planar ultraviolet photonic device applications. Adv. Mater. 28. 8446–8454 (2016).
- Y.-H. Ra, R. Wang, S. Y. Woo, M. Djavid, S. M. Sadaf, J. Lee, G. A. Botton, Z. Mi, Full-color single nanowire pixels for projection displays. *Nano Lett.* 16, 4608–4615 (2016).
- H. P. Nguyen, S. Zhang, A. T. Connie, M. G. Kibria, Q. Wang, I. Shih, Z. Mi, Breaking the carrier injection bottleneck of phosphor-free nanowire white light-emitting diodes. *Nano Lett.* 13, 5437–5442 (2013).
- H. P. Nguyen, M. Djavid, S. Y. Woo, X. Liu, A. T. Connie, S. Sadaf, Q. Wang, G. A. Botton, I. Shih, Z. Mi, Engineering the carrier dynamics of InGaN nanowire white light-emitting diodes by distributed p-AlGaN electron blocking layers. Sci. Rep. 5, 7744 (2015).
- A. E. Romanov, T. J. Baker, S. Nakamura, J. S. Speck; ERATO/JST UCSB Group, Straininduced polarization in wurtzite III-nitride semipolar layers. J. Appl. Phys. 100, 023522 (2006).
- M. Pristovsek, Y. Han, T. Zhu, M. Frentrup, M. J. Kappers, C. J. Humphreys, G. Kozlowski, P. Maaskant, B. Corbett, Low defect large area semi-polar (112 2) GaN grown on patterned (113) silicon. *Phys. Status Solidi B* 252, 1104–1108 (2015).
- T. Wang, Topical review: Development of overgrown semi-polar GaN for high efficiency green/yellow emission. Semicond. Sci. Technol. 31, 093003 (2016).
- K. Kishino, S. Ishizawa, Selective-area growth of GaN nanocolumns on Si(111) substrates for application to nanocolumn emitters with systematic analysis of dislocation filtering effect of nanocolumns. *Nanotechnology* 26, 225602 (2015).
- J. Wallentin, M. T. Borgström, Doping of semiconductor nanowires. J. Mater. Res. 26, 2142–2156 (2011).
- P. S. Yeh, C.-C. Chang, Y.-T. Chen, D.-W. Lin, J.-S. Liou, C. C. Wu, J. H. He, H.-C. Kuo, GaN-based vertical-cavity surface emitting lasers with sub-milliamp threshold and small divergence angle. *Appl. Phys. Lett.* **109**, 241103 (2016).
- T. Hamaguchi, N. Fuutagawa, S. Izumi, M. Murayama, H. Narui, Milliwatt-class GaN-based blue vertical-cavity surface-emitting lasers fabricated by epitaxial lateral overgrowth. *Phys. Status Solidi A* 213, 1170–1176 (2016).

# SCIENCE ADVANCES | RESEARCH ARTICLE

- D. F. Feezell, Status and future of GaN-based vertical-cavity surface-emitting lasers, in Proceedings of SPIE, Gallium Nitride Materials and Devices X (13 March 2015), vol. 9363, pp. 93631G.
- F. E. Veiras, L. M. Riobó, C. L. Matteo, L. I. Perez, M. T. Garea, Birefringent phase demodulator: Application to wave plate characterization. *Appl. Optics* 54, 2326–2333 (2015).
- P. J. W. Hands, S. M. Morris, T. D. Wilkinson, H. J. Coles, Two-dimensional liquid crystal laser array. Opt. Lett. 33, 515–517 (2008).
- N. A. Mortensen, J. R. Folkenberg, Near-field to far-field transition of photonic crystal fibers: Symmetries and interference phenomena. Opt. Express 10, 475–481 (2002).
- H.-G. Park, S.-H. Kim, S.-H. Kwon, Y.-G. Ju, J.-K. Yang, J.-H. Baek, S.-B. Kim, Y.-H. Lee, Electrically driven single-cell photonic crystal laser. Science 305, 1444–1447 (2004).
- C. Li, J. B. Wright, S. Liu, P. Lu, J. J. Figiel, B. Leung, W. W. Chow, I. Brener, D. D. Koleske, T.-S. Luk, D. F. Feezell, S. R. J. Brueck, G. T. Wang, Nonpolar InGaN/GaN core-shell single nanowire lasers. *Nano Lett.* 17, 1049–1055 (2017).
- X. M. Xi, T. Weiss, G. K. L. Wong, F. Biancalana, S. M. Barnett, M. J. Padgett, P. St. J. Russell, Optical activity in twisted solid-core photonic crystal fibers. *Phys. Rev. Lett.* 110, 143903 (2013)
- M. J. Bergmann, H. C. Casey Jr., Optical-field calculations for lossy multiple-layer Al<sub>x</sub>Ga<sub>1-x</sub>N/In<sub>x</sub>Ga<sub>1-x</sub>N laser diodes. *J. Appl. Phys.* 84, 1196–1203 (1998).
- A. B. Djurišić, E. H. Li, Modeling the optical constants of hexagonal GaN, InN, and AIN. J. Appl. Phys. 85, 2848–2853 (1999).
- C.-Y. Huang, Y.-D. Lin, A. Tyagi, A. Chakraborty, H. Ohta, J. S. Speck, S. P. DenBaars, S. Nakamura, Optical waveguide simulations for the optimization of InGaN-based green laser diodes. *J. Appl. Phys.* **107**, 023101 (2010).
- N. A. Sanford, L. H. Robins, A. V. Davydov, A. Shapiro, D. V. Tsvetkov, A. V. Dmitriev, S. Keller, U. K. Mishra, S. P. DenBaars, Refractive index study of Al<sub>x</sub>Ga<sub>1-x</sub>N films grown on sapphire substrates. *J. Appl. Phys.* 94, 2980–2991 (2003).
- R. Wang, X. Liu, I. Shih, Z. Mi, High efficiency, full-color AllnGaN quaternary nanowire light emitting diodes with spontaneous core-shell structures on Si. Appl. Phys. Lett. 106, 261104 (2015).
- S. M. Sadaf, S. Zhao, Y. Wu, Y.-H. Ra, X. Liu, S. Vanka, Z. Mi, An AlGaN core–shell tunnel junction nanowire light-emitting diode operating in the ultraviolet-C band. *Nano Lett.* 17, 1212–1218 (2017).
- K. Hestroffer, C. Leclere, C. Bougerol, H. Renevier, B. Daudin, Polarity of GaN nanowires grown by plasma-assisted molecular beam epitaxy on Si(111). *Phys. Rev. B* 84, 245302 (2011).
- X. J. Chen, G. Perillat-Merceroz, D. Sam-Giao, C. Durand, J. Eymery, Homoepitaxial growth of catalyst-free GaN wires on N-polar substrates. Appl. Phys. Lett. 97, 151909 (2010).
- X. Q. Shen, T. Ide, M. Shimizu, H. Okumura, Growth and characterizations of InGaN on N- and Ga-polarity GaN grown by plasma-assisted molecular-beam epitaxy. J. Cryst. Growth 237-239, 1148–1152 (2002).

- S. Fernández-Garrido, X. Kong, T. Gotschke, R. Calarco, L. Geelhaar, A. Trampert, O. Brandt, Spontaneous nucleation and growth of GaN nanowires: The fundamental role of crystal polarity. *Nano Lett.* 12, 6119–6125 (2012).
- P.-M. Coulon, B. Alloing, V. Brändli, D. Lefebvre, S. Chenot, J. Zúñiga-Pérez, Selective area growth of Ga-polar GaN nanowire arrays by continuous-flow MOVPE: A systematic study on the effect of growth conditions on the array properties. *Phys. Status Solidi B* 252, 1096–1103 (2015).
- S. Y. Kim, H. W. Jang, J.-L. Lee, Effect of an indium-tin-oxide overlayer on transparent Ni/Au ohmic contact on p -type GaN. Appl. Phys. Lett. 82, 61–63 (2003).
- J.-S. Jang, S.-J. Park, T.-Y. Seong, Ultrahigh transparency of Ni/Au ohmic contacts to surface-treated p-type GaN. J. Appl. Phys. 88, 5490–5492 (2000).
- S. W. Chae, J. S. Kwak, S. K. Yoon, M. Y. Kim, J. O. Song, T. Y. Seong, T. G. Kim, Characteristics of hydrogen storage alloy p-GaN ohmic contacts for InGaN LEDs. J. Korean Phys. Soc. 49. 899 (2006).
- W. Hou, C. Stark, S. You, L. Zhao, T. Detchprohm, C. Wetzel, Evaluation of metal/ indium-tin-oxide for transparent low-resistance contacts to p-type GaN. Appl. Optics 51, 5596–5600 (2012).

#### Acknowledgments

Funding: This work was supported by the U.S. Army Research Office (W911NF-17-1-0388) and NSF (ECCS-1709207). Author contributions: Y.-H.R. and Z.M. conceived the ideas. R.T.R. and Y.-H.R. fabricated the nanopatterned mask substrates. Y.-H.R. conducted the MBE growths. Y.-H.R. and R.T.R. performed SEM and PL measurements. Y.-H.R. contributed to the TEM analysis and carried out the device fabrication. Y.-H.R. and S.M.S. performed the electrical and optical characterization. X.L. and K.M. contributed to the theoretical simulation. Y.-H.R. and Z.M. wrote the manuscript with contributions from other co-authors. Competing interests: Y.-H.R., R.T.R., X.L., and Z.M. are inventors on a patent application related to this work (no. 62/915,432, date filed: 15 October 2019). Intellectual property related to this work has been licensed to NS Nanotech Inc., which was co-founded by Z.M. The authors declare that they have no other competing interests. Data and materials availability: All data needed to evaluate the conclusions in the paper are present in the paper and/or the Supplementary Materials. Additional data related to this paper may be requested from the authors.

Submitted 16 October 2018 Accepted 29 October 2019 Published 3 January 2020 10.1126/sciadv.aav7523

Citation: Y.-H. Ra, R. T. Rashid, X. Liu, S. M. Sadaf, K. Mashooq, Z. Mi, An electrically pumped surface-emitting semiconductor green laser. *Sci. Adv.* 6, eaav7523 (2020).



## An electrically pumped surface-emitting semiconductor green laser

Yong-Ho Ra, Roksana Tonny Rashid, Xianhe Liu, Sharif Md. Sadaf, Kishwar Mashoog and Zetian Mi

Sci Adv **6** (1), eaav7523. DOI: 10.1126/sciadv.aav7523

ARTICLE TOOLS http://advances.sciencemag.org/content/6/1/eaav7523

SUPPLEMENTARY http://advances.sciencemag.org/content/suppl/2019/12/20/6.1.eaav7523.DC1

**REFERENCES** This article cites 81 articles, 2 of which you can access for free

http://advances.sciencemag.org/content/6/1/eaav7523#BIBL

PERMISSIONS http://www.sciencemag.org/help/reprints-and-permissions

Use of this article is subject to the Terms of Service